Thin Cloud Correction for Single Optical Satellite Image Using Complementary Dark Objects on Multiple Visible Bands

Peng Yi, Chi Zhang, *Member, IEEE*, Li Ma, Yang Liu, Huagui He, and Wenxiong Hu

***Abstract*—Optical satellite images frequently suffer from thin clouds, degrading the data quality. A thin cloud correction method is developed based on complementary dark objects on multiple visible bands to address this problem. First, thin cloud images are divided into irregular subareas using the superpixel segmentation algorithm, enabling the proper identification of dark objects in the spatial domain across different visible bands. A criterion is then established to classify the dark objects into two types, namely, absolute dark objects (ADOs) and relative dark objects (RDOs). Subsequently, the quantitative correlation of thin clouds between visible bands is estimated by adopting the ADOs. Dark objects present complementarity in visible bands; thus, the RDOs on one band are spatially densified by referencing the RDOs on the other visible bands. Thereby, a thin cloud map with fine spatial details is interpolated by using all the ADOs and RDOs on a band, and the correction procedure is performed through subtraction. Eight visible data captured by Landsat platforms are collected for simulated and real experiments to evaluate the method's performance. Three representative thin cloud correction approaches are selected for visual and quantitative comparisons. The proposed method can correct thin clouds effectively and restore various scenes accurately. The interpolated thin cloud maps show enhanced texture details and finer representation compared with the benchmarks. In addition, the advantages of dark-object densification for thin cloud map generation and the limitations of the proposed method are investigated.**

***Index Terms*—Band correlation, complementary dark object, optical satellite image, spatial interpolation, thin cloud correction.**

I. Introduction

THIN clouds pose a considerable challenge to optical remote sensing observations because they are semitransparent, highly reflective, and usually tend to exhibit slow spatial variation in satellite views [1]. These characteristics cause thin cloud-covered regions to appear brighter than their surroundings, containing radiation from clouds and land surfaces. In some cases, thick clouds are present in the scene at the same time, which are opaque and out of the scope of this article [2], [3]. Consequently, correction procedures are necessary for cloud-contaminated images before the images are applied in real applications, such as natural resource monitoring, land cover change detection, and regional environmental evaluation.

Numerous efforts have been made to address the issue of thin clouds in optical satellite images, particularly in the visible bands. This study focuses on thin cloud correction in the visible bands and categorizes the existing approaches into four main types: deep-learning-based, frequency-domain filter-based, spectral-correlation-based, and dark-object-based methods. Deep-learning-based methods aim to map thin cloud images to cloud-free images through nonlinear transformations, optimizing transformation parameters using large-scale datasets via backpropagation [4], [5], [6]. Convolutional neural networks and generative adversarial networks are popular architectures, and variations, such as residual symmetrical concatenation network [7], residual learning and channel attention mechanism (RLCAM) integrated network [8], and attention mechanism-based generative adversarial network [9], have been designed for thin cloud correction tasks. Although these methods show promising performance, they rely heavily on robust network structures and large datasets for optimal results, limiting their practicality, especially in emergency cases with limited data.

Unlike deep-learning-based methods, the other three categories of approaches rely solely on information from the image itself and do not need pretraining, thus being more practical. Frequency-domain filter-based methods assume that thin clouds correspond to low-frequency components due to their spatial smoothness, while land surfaces, which are rich in textures, are considered high-frequency components. These methods convert thin cloud images to the frequency domain and remove thin clouds using homomorphic filtering [1] and other high-pass filters [10], [11], [12], [13]. Although frequency-domain filter-based methods do not have specific data requirements and are suitable for various types of optical images, they suffer from certain limitations. For instance, smooth land covers, such as uniform water surfaces, might be mistakenly treated as thin

Manuscript received 15 August 2023; revised 18 December 2023; accepted 28 January 2024. Date of publication 21 February 2024; date of current version 13 March 2024. This work was supported in part by the Guangzhou Collaborative Innovation Center of Natural Resources Planning and Marine Technology under Grant 2023B04J0301, in part by the Key-Area Research and Development Program of Guangdong Province under Grant 2020B0101130009, in part by the Guangdong Enterprise Key Laboratory for Urban Sensing, Monitoring, and Early Warning under Grant 2020B121202019, and in part by the Science and Technology Foundation of Guangzhou Urban Planning and Design Survey Research Institute (RD No. 2220201132 and 2230201025). *(Corresponding authors: Chi Zhang; Yang Liu.)*

The authors are with the Guangzhou Urban Planning and Design Survey Research Institute, Guangzhou 510060, China, and also with the Guangdong Enterprise Key Laboratory for Urban Sensing, Monitoring and Early Warning, Guangzhou 510060, China (e-mail: kalma@163.com; zhangchi9502@outlook.com; pppmali@126.com; liuyang_052@163.com; gzhehuagui@163.com; 251125113@qq.com).

Digital Object Identifier 10.1109/JSTARS.2024.3366178

clouds and subsequently corrected, leading to color distortion in the resulting images. Spectral-correlation-based methods are employed to distinguish between thin clouds and land surfaces based on their different correlations across bands. Representative techniques include haze-optimized transformation [14], linear band transformation [15], tasseled cap transformation [16], independent component analysis [17], principal component analysis [18], and principal component transformation [19]. These methods require pending thin cloud images that consist of data from at least two bands to perform the spectral transformations.

Dark-object-based methods rely on the existence of pixels with very low reflectance, known as dark objects, in one or several bands. Dark objects are real and widespread on the Earth's surfaces, making this category of methods more practical and applicable compared with the other three categories. Several milestone approaches and their variants have been developed for correcting thin clouds in visible satellite data. These methods include primeval dark-object subtraction (PDOS) [20], improved dark-object subtraction (IDOS) [21], haze thickness map (HTM) [22], dark channel prior (DCP) [23], and spatial–spectral adaptive dark channel prior (SSADCP) [24]. PDOS is an early method that uses dark objects to correct uniform thin clouds in individual bands. Building upon this method, IDOS extends the correction scope from the individual band to multiple visible bands by introducing the scattering law. HTM further optimizes the search strategy of dark objects from a global to a local scale, leading to finer thin cloud maps for each band. DCP can be regarded as an enhanced version of HTM, as it extends the search for dark objects from band-by-band to multibands, promising an increased number of dark objects and improved cloud correction performance. However, DCP has limitations because it ignores the band varying of thin clouds and may be sensitive to bright surfaces lacking dark objects. SSADCP achieves substantial progress by proposing a band-varied thin cloud estimation approach and developing a spatial adaptive strategy, which helps address the adverse effects of cloud varying and bright surfaces to some extent. In summary, dark-object-based methods have proven to be efficient for correcting thin clouds in visible satellite data. However, their performance heavily relies on the density of dark objects in the spatial domain. When dark objects are spatially sparse, the accurate estimation of thin clouds becomes challenging, leading to overcorrection or undercorrection in the results.

From the above findings, dark-object-based methods are more practical and widely applicable, often yielding satisfactory results compared with the other three categories of methods. This is because dark objects are real and commonly found on the Earth's surfaces, making the assumption of their existence reliable and robust. Representative land covers that contain dark objects include dark soils, shadows, and dense vegetation. However, as mentioned previously, the efficiency of dark-object-based methods is limited by the spatial density of dark objects. Theoretically, denser distribution of dark objects leads to finer thin cloud maps and better results. This study explores and exploits the complementarity of dark objects across multiple visible bands to densify their spatial distribution, based on which a thin cloud correction method is designed for a single optical satellite image. The major contributions of this article are as follows.

1) A novel thin cloud correction method was proposed for a single optical satellite, which is simple but effective. This study explores and exploits the complementarity of dark objects across multiple visible bands to generate a thin cloud map with fine details, ensuring the satisfactory performance for various satellite data.
2) A criterion to classify dark objects was established. Two subconcepts—absolute dark objects (ADOs) and relative dark objects (RDOs)—were further defined to characterize the dark objects.
3) A robust estimation strategy for estimating the band correlation of thin clouds was developed based on ADOs. A spatial densification strategy for dark objects was developed by referring to RDOs.

The rest of this article is organized as follows. Section II gives the details of the proposed method. Section III provides the experimental results and the comparison with other benchmark methods. Section IV discusses the advantages and limitations of the method. Finally, Section V concludes this article.

II. Method

The accurate estimation of thin cloud intensity for each visible band is a necessary precondition for cloud correction [25]. In this study, the complementarity of dark objects across multiple visible bands is investigated and utilized to spatially densify their distribution. A finely detailed thin cloud map can be generated by doing so, promising precise cloud correction. The method's outline is given as follows. Thin cloud images are divided into irregular subareas via superpixel segmentation. Dark objects are identified within subareas in different visible bands. A criterion is then constructed to classify the dark objects into two types: ADOs and RDOs. The band correlation of thin cloud intensity is calculated using ADOs. Given the complementarity of dark objects, the RDOs on a band are densified by referencing the RDOs on the other bands. All the ADOs and densified RDOs on a band are utilized to generate the thin cloud map using spatial interpolation. Thin cloud correction is performed through subtraction. Correspondingly, an overall flowchart of the proposed method is provided in Fig. 1.

A. Empirical Cloudy Image Model

Optical satellite images captured under a turbid atmosphere are typically modeled as follows [26], [27]:

$$\rho^* = \rho + \rho_c \tag{1}$$

where ρ represents the land surface underneath thin clouds. ρ_c denotes the thin clouds, mainly triggered by scattering effects [28]. ρ^* is the observed thin cloud image. The correction procedure in this study is based on (1).

Thin cloud problem in visible bands is more severe and of greater concern than in other bands due to the stronger scattering effects. Quantitatively, the scattering effects can be described by scattering law [29], [30]. On this basis, the thin cloud intensity between arbitrary pairs of visible bands i and j can be

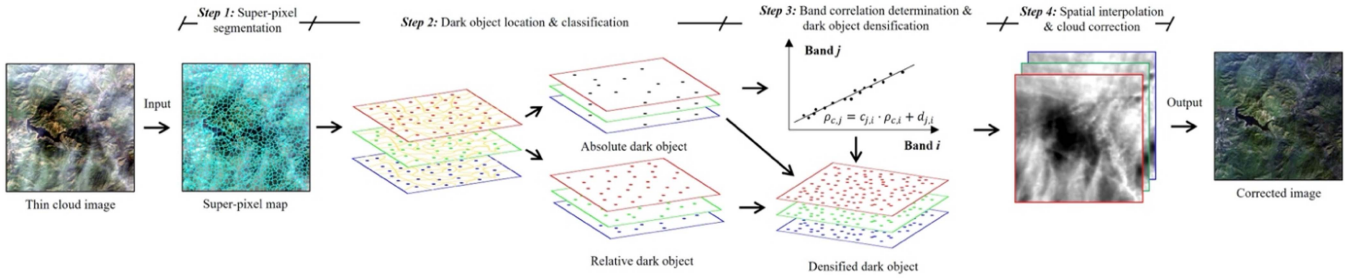

Fig. 1. Overall flowchart of the proposed method.

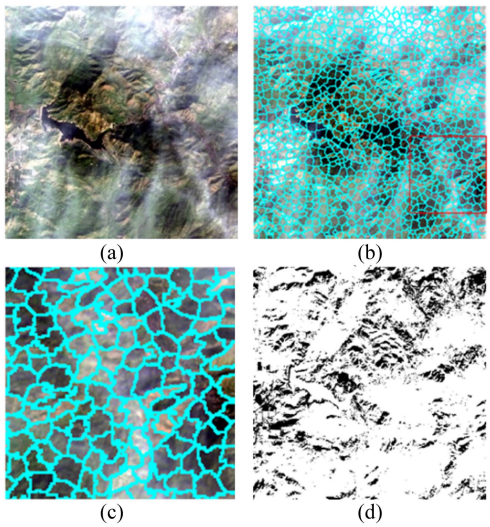

Fig. 2. Instance of thin cloud image segmentation using the simple linear iterative clustering algorithm. (a) Thin cloud image acquired by Landsat 8 on 13 February 2022 (path: 042 and row: 035). (b) Result of superpixel segmentation. (c) Enlarged version of the red rectangle in (b). (d) Binarized BPI map in which the black areas are the identified bright surfaces.

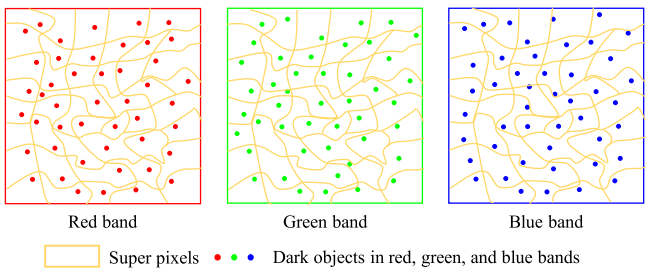

Fig. 3. Illustration of dark-object location in different superpixels on each visible band.

derived as follows [21]:

$$\rho_{c,i} = a_{i,j} \cdot \rho_{c,j} \tag{2}$$

where $a_{i,j}$ is the correlation coefficient (CC). Equation (2) denotes that the thin cloud intensity between any pair of visible bands is directly proportional to each other.

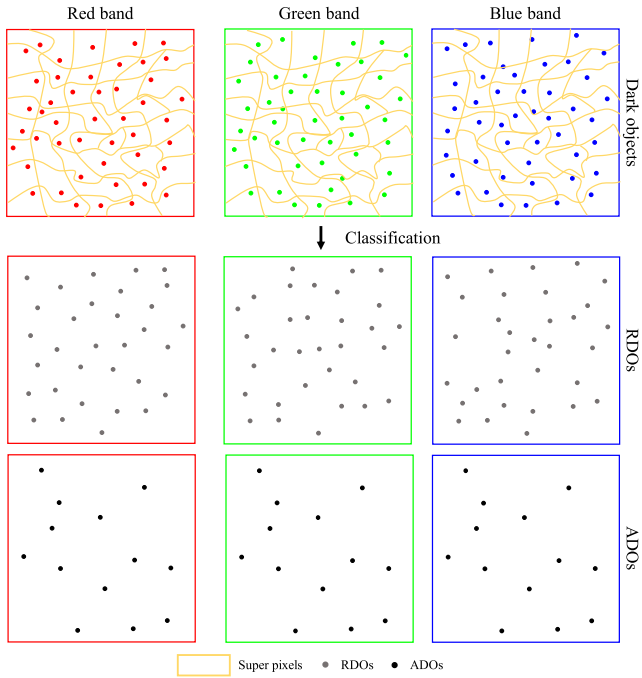

Fig. 4. Flowchart of dark-object classification.

B. Location of Dark Objects Based on Superpixel Segmentation

Dark objects in local areas on different visible bands need to be located before thin cloud estimation. The existing methods usually divide cloudy images into several nonoverlapping or overlapped rectangular subareas and consider the pixel with the minimum value in each subarea as the dark object [22], [23], [24]. However, in reality, thin clouds are not always constant in a rectangular patch [23]. In addition, a rectangular subarea may contain multiple land covers. Although the dark objects from different land covers all have very low reflectance, their inherent reflectance is not completely the same [21]. Consequently, the thin cloud intensity estimated by the dark object from one land cover is unsuitable for characterizing the thin cloud intensity of the other land covers in the same rectangular subarea. Thus, the distribution of land covers needs to be considered when dividing thin cloud images for locating dark objects.

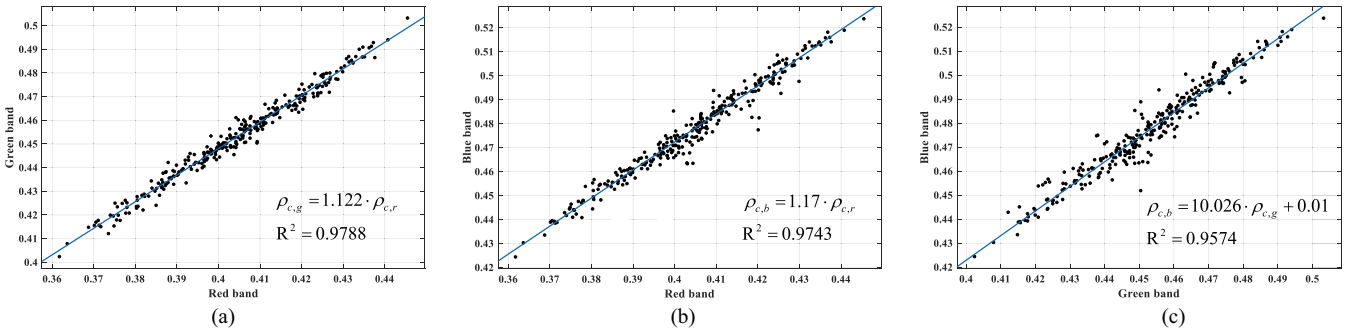

Fig. 5. Linear regression results of ADOs between an arbitrary pair of visible bands. (a) Red band versus green band. (b) Red band versus blue band. (c) Green band versus blue band.

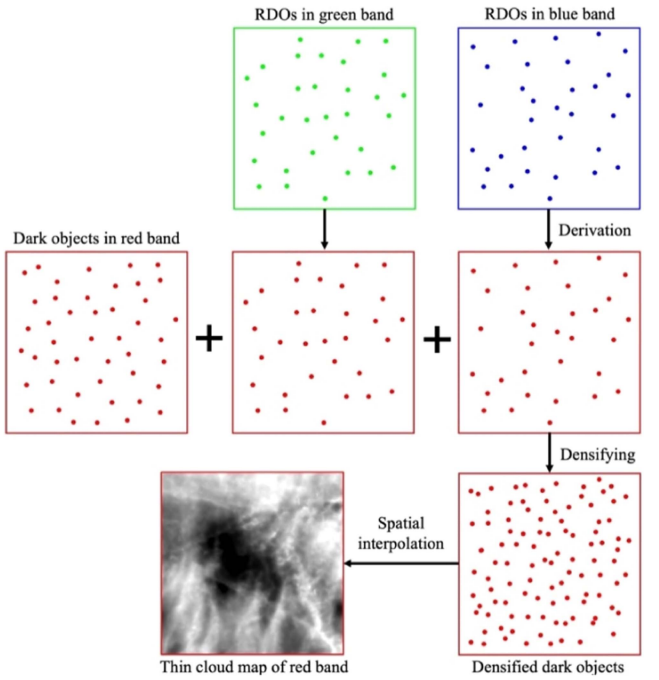

Fig. 6. Illustration of dark-object densification and thin cloud map interpolation using the red band as an example.

Given that an arbitrary land cover consists of pixels with similar spectral and texture features, superpixel segmentation can be used to perform image division oriented to land covers. The simple linear iterative clustering algorithm is adopted in this study. An instance of superpixel segmentation for a thin cloud image is illustrated in Fig. 2. The image size in Fig. 2(a) is 512 pixels × 512 pixels, and the number of superpixels in Fig. 2(b) is 1024. In each superpixel, the pixels with minimum values in different visible bands are located and labeled as dark objects, as shown in Fig. 3. However, in some cases, pixels from bright surfaces, such as bare soils, might be wrongly defined as dark objects, leading to the misestimation of thin clouds. The bright pixel index (BPI) proposed in previous work is adopted to solve this problem [24]. The BPI values of bright surfaces are always much lower than those of other land covers, which provides a clue to exclude them [see Fig. 2(d)]. Each superpixel represents only one land cover; thus, the thin cloud intensity in different superpixels can be properly characterized by the located dark objects.

C. Spatial Densification of Dark Objects in Visible Bands

Dark objects refer to pixels with very low reflectance in a band or multiple bands, mainly from two categories of land covers. One category is dark soils, shadows, and dense vegetation, which have low reflectance in all visible bands. The other category refers to some colorful ground features, which have low reflectance in at least one visible band. For example, the reflectance of blue roofs is high in the blue band but low in the other green and red bands. The pixels from the former category are always labeled as dark objects in all visible bands and are classified as ADOs in this study. Those from the latter category are labeled in only one or several visible bands and are defined as RDOs. The classification of dark objects is illustrated in the flowchart in Fig. 4.

For ADOs, ρ is close to zero in all visible bands, and ρ^* can be regarded as equal to ρ_c, that is, $\rho^* = \rho_c$. Therefore, the band correlation of thin clouds can be obtained by linearly fitting the ADOs from different band pairs, which can be expressed as

$$\rho_{c,k} = c_{k,l} \cdot \rho_{c,l} + d_{k,l} \tag{3}$$

where the subscripts k and l represent a pair of visible bands, and c and d are the linear fitting coefficients. $c_{k,l}$ represents the proportionality coefficient of thin cloud intensity between visible bands k and l and equals $a_{i,j}$ in (2). $d_{k,l}$ is related to the reflectance of dark objects under clear sky conditions.

With the thin cloud image in Fig. 2(a) taken as an example again, the linear regressions of ADOs from different band pairs are executed and plotted in Fig. 5. As the figures show, the scatter points are highly clustered around the fitting lines. The coefficient of determination R^2 varies from 0.9574 to 0.9788, demonstrating a remarkable linear correlation. In addition, parameter d is 0, 0, and 0.01 in the three linear relations, respectively. This finding proves that the ADOs are truly dark in all visible bands, but their inherent reflectance is not exactly the same under clear sky conditions.

Unlike ADOs, RDOs have low reflectance in one or several visible bands and can accurately characterize the thin cloud

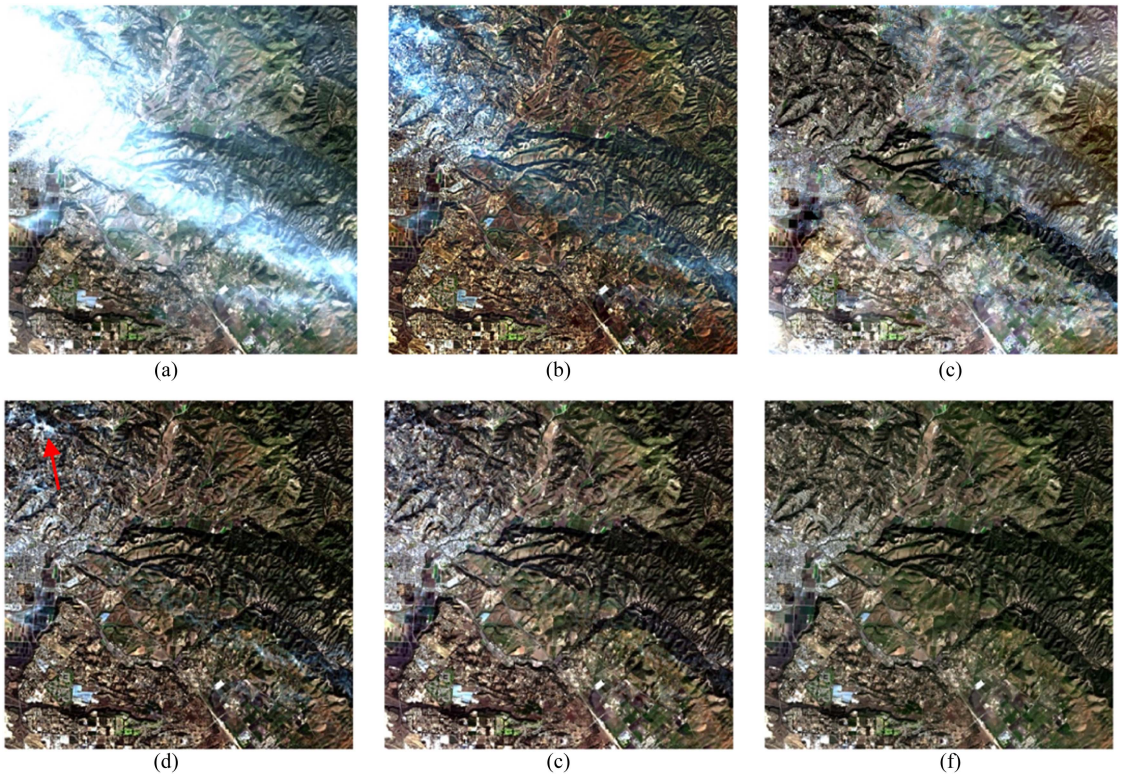

Fig. 7. Thin cloud correction results of the first simulated data using different methods. (a) First simulated thin cloud data. (b) RLCAM. (c) NAPCT. (d) SSADCP. (e) Proposed method. (f) Cloud-free image.

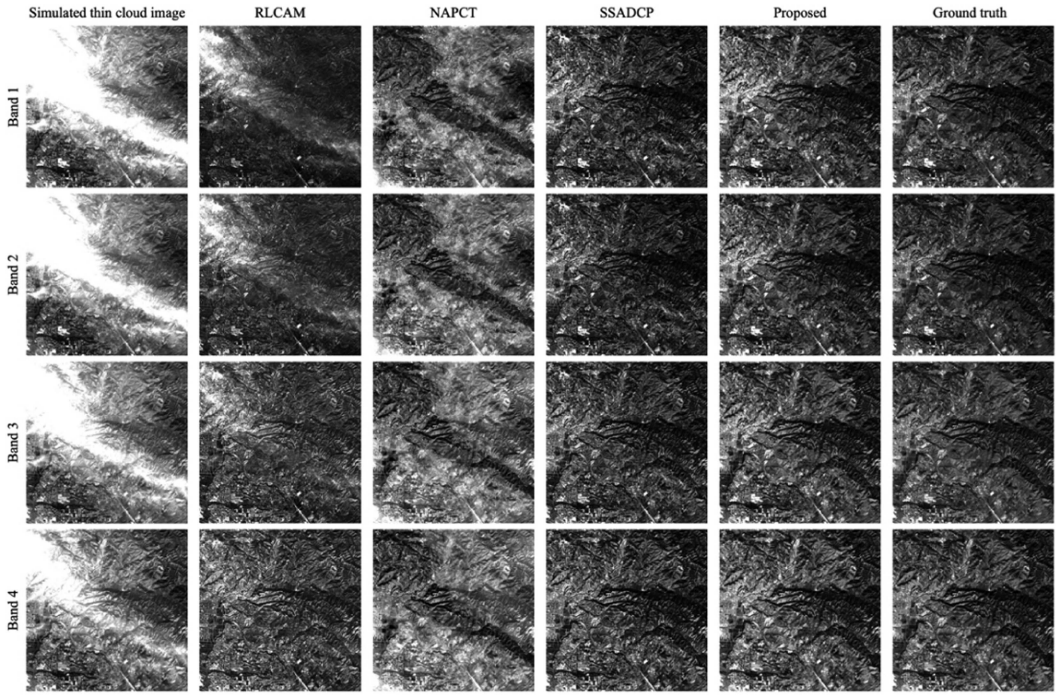

Fig. 8. Band-by-band comparison of different results. The first to the sixth columns show the visible bands (Bands 1–4 of OLI) of the simulated thin cloud image RLCAM, NAPCT, SSADCP, the proposed method, and the ground truth, respectively.

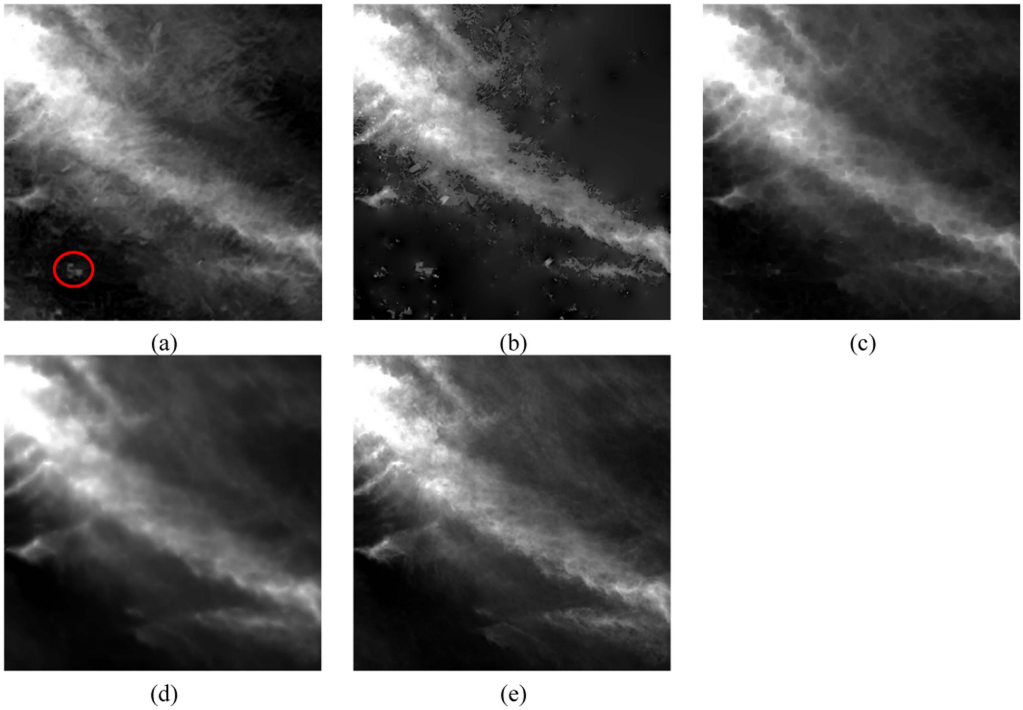

Fig. 9. Thin cloud maps produced by different methods. (a)–(d) Exhibit the thin cloud maps generated from RLCAM, NAPCT, SSADCP, and the proposed method. (e) Ground truth.

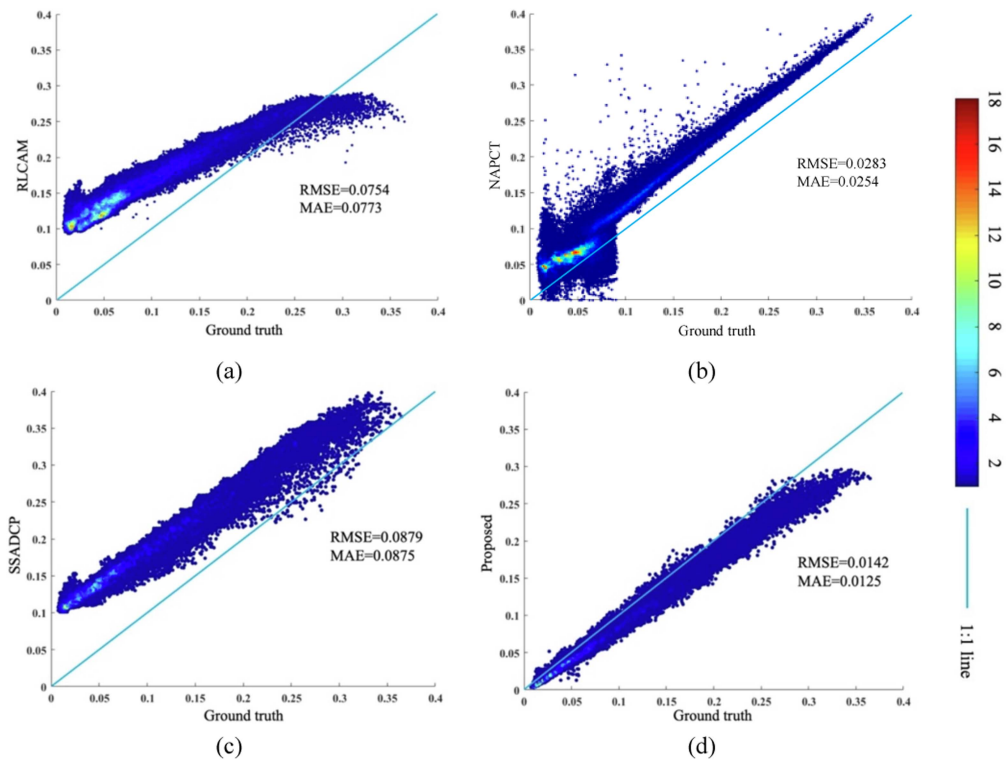

Fig. 10. Scatter plots between different thin cloud maps and the ground truth. (a) Ground truth versus RLCAM. (b) Ground truth versus NAPCT. (c) Ground truth versus SSADCP. (d) Ground truth versus the proposed method.

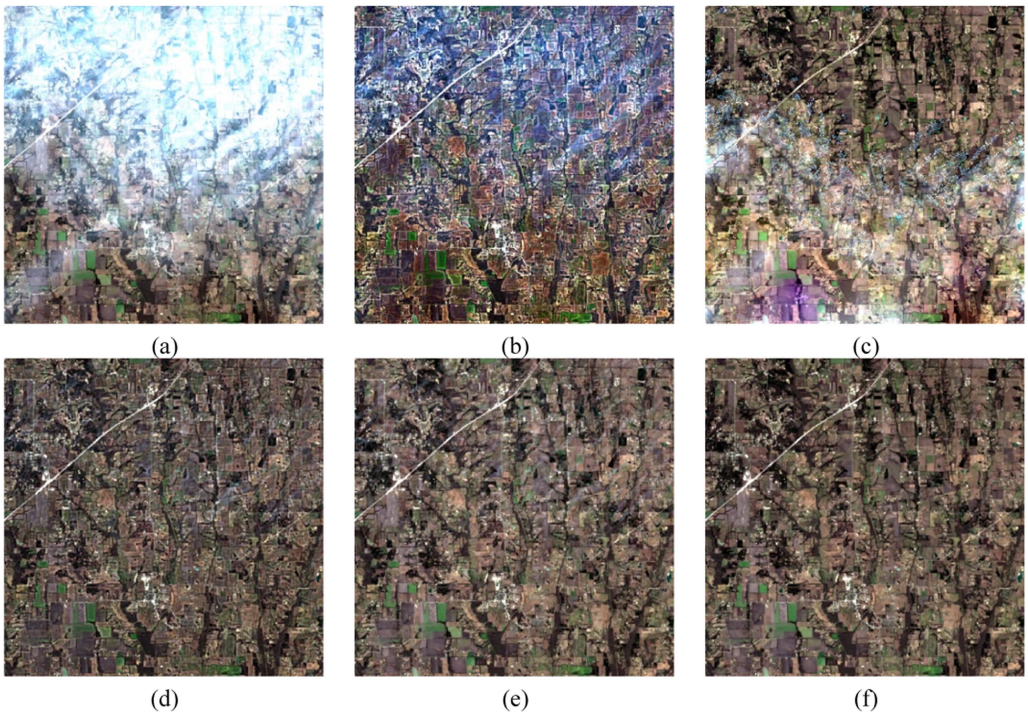

Fig. 11. Thin cloud correction results of the second simulated data using different methods. (a) Second simulated thin cloud data. (b) RLCAM. (c) NAPCT. (d) SSADCP. (e) Proposed method. (f) Cloud-free image.

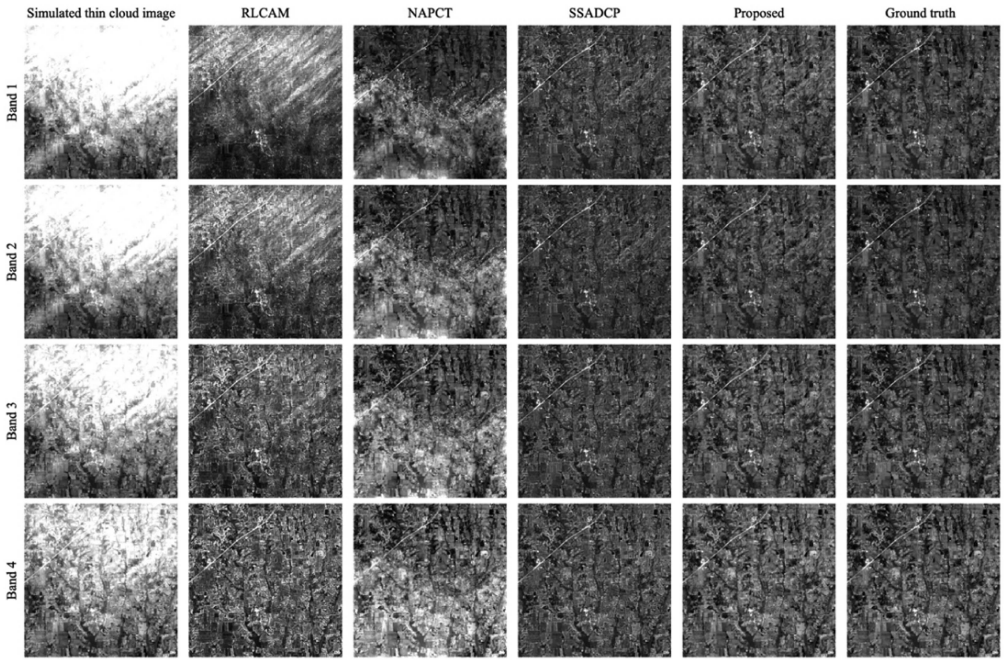

Fig. 12. Band-by-band comparison of different results. The first to the sixth columns show the visible bands (Bands 1–4 of OLI) of the simulated thin cloud image, RLCAM, NAPCT, SSADCP, proposed method, and ground truth, respectively.

intensity in the corresponding bands. The relation of thin cloud intensity between visible bands is obtained from (3), based on which the RDOs in a band can be used to derive the virtual RDOs at the same positions in the other bands. With the red band taken as an example, the derivation of virtual RDOs from the green band is expressed as

$$\rho_{c,r} = c_{r,g} \cdot \rho_{c,g} \tag{4}$$

where $c_{r,g}$ represents the proportionality coefficient of the thin cloud intensity between the red and green bands. Similarly, the

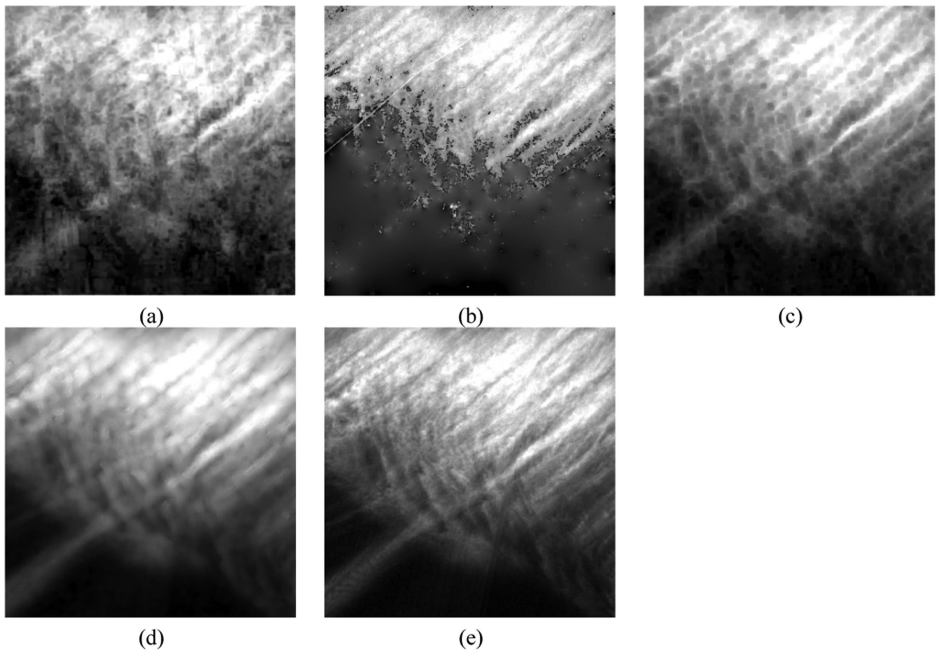

Fig. 13. Thin cloud maps produced by different methods. (a)–(d) Exhibit the thin cloud maps generated from RLCAM, NAPCT, SSADCP, and the proposed method. (e) Ground truth.

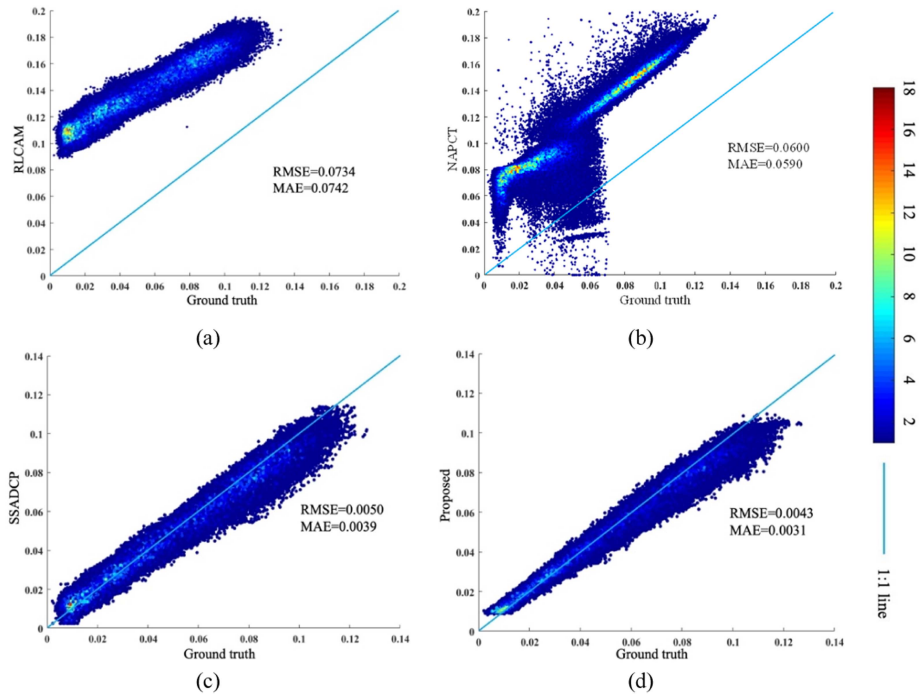

Fig. 14. Scatter plots between different thin cloud maps and ground truth. (a) Ground truth versus RLCAM. (b) Ground truth versus NAPCT. (c) Ground truth versus SSADCP. (d) Ground truth versus the proposed method.

derivation from the blue band is given as follows:

$$\rho_{c,r} = c_{r,b} \cdot \rho_{c,b}. \tag{5}$$

Thus, the RDOs on a band can be densified by taking the RDOs on the other bands as a reference based on the complementarity of dark objects. All the ADOs and densified RDOs in a band are then used to interpolate a spatially continuous thin cloud map, which should have fine texture details.

The illustration of the dark-object densification and thin cloud map interpolation is exhibited in Fig. 6. As long as the thin cloud intensity for each visible band is accurately estimated, the thin cloud correction can be completed through subtraction.

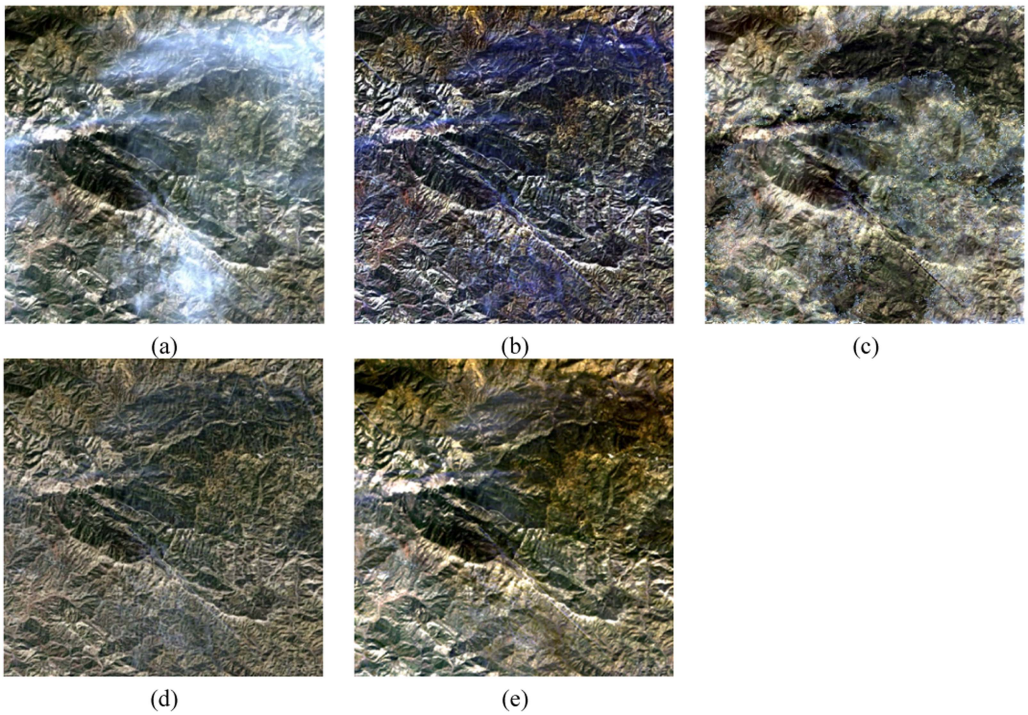

Fig. 15. Thin cloud correction results of the first real data using different methods, with acquired data from 26 March 2022 (path: 042 and row: 036). (a) First real thin cloud data. (b) RLCAM. (c) NAPCT. (d) SSADCP. (e) Proposed method.

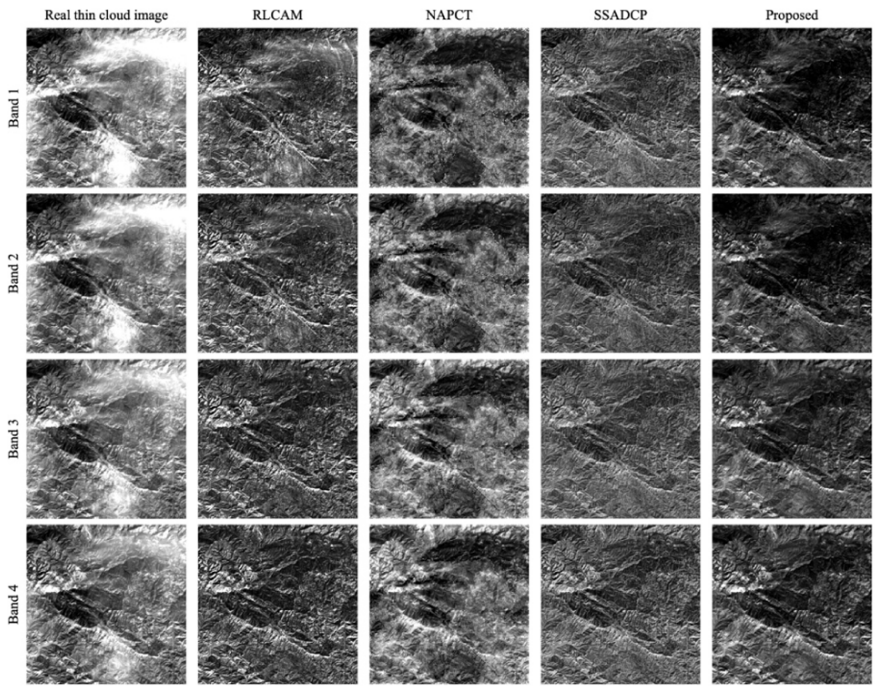

Fig. 16. Band-by-band comparison of different results. The first to the fifth columns show the visible bands (Bands 1–4 of OLI) of the real thin cloud image, RLCAM, NAPCT, SSADCP, and proposed method, respectively.

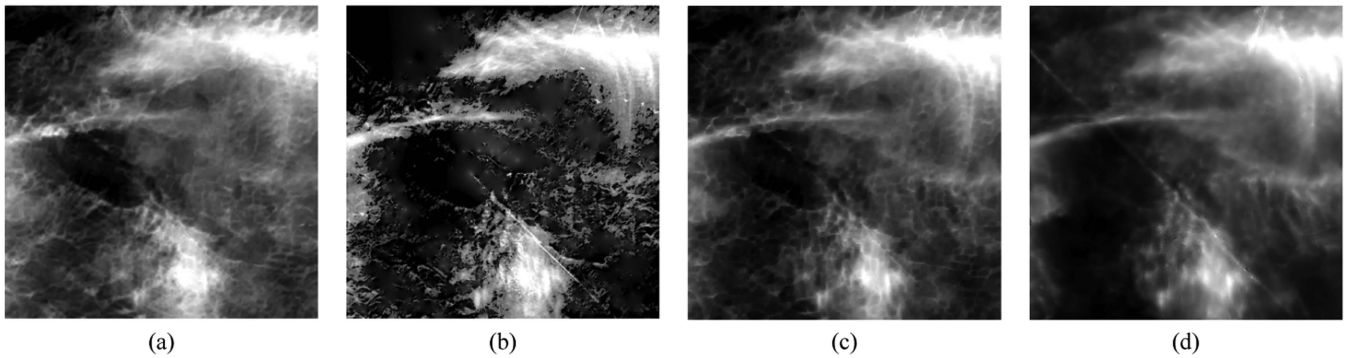

Fig. 17. Comparison of thin cloud maps produced by different methods. (a)–(d) Exhibit the thin cloud map generated from RLCAM, NAPCT, SSADCP, and the proposed method.

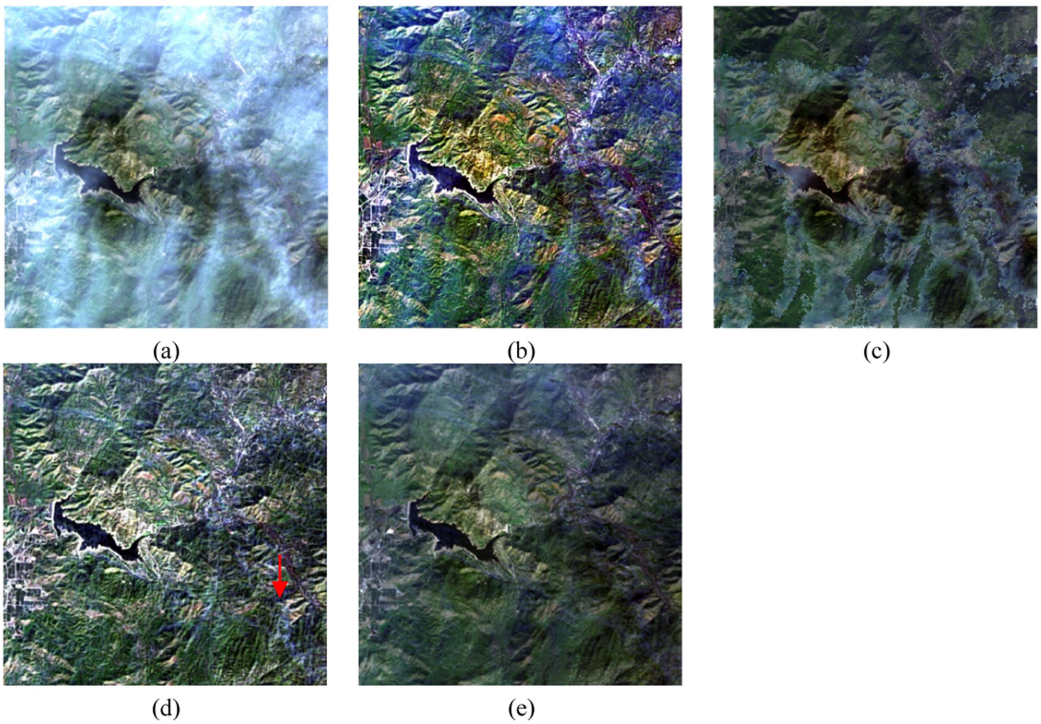

Fig. 18. Thin cloud correction results of the second real data using different methods, with acquired data from 13 February 2022 (path: 042 and row: 035). (a) Second real thin cloud image. (b) RLCAM. (c) NAPCT. (d) SSADCP. (e) Proposed method.

III. Experiments

Two simulated and six real thin cloud images are collected from Landsat 9 operational land imager2 (OLI2), Landsat 8 OLI, and Landsat 7 enhanced thematic mapper plus (ETM+) to validate the cloud correction performance of the proposed method. The experimental data contain various scenes, including forests, mountainous regions, bare soils, and water areas. Three representative thin cloud correction methods, namely, RLCAM-integrated network [8], principal component analysis (NAPCT) [19], and SSADCP [24], are selected as benchmarks for comparison. Result evaluations are executed from visual and quantitative aspects. Visually, the corrected results of different methods are checked band-by-band, and the thin cloud maps are compared. Quantitatively, four metrics, namely, root-mean-square error (RMSE), mean absolute error (MAE), CC, and spectral angle (SA) are computed to assess the data accuracy.

A. Simulated Experiments

In accordance with the work of Zhang et al.[28], the generation of simulated thin cloud images refers to the empirical cloudy image model in (1). The clear surfaces ρ are from the scene captured under a clear sky. Thin cloud masks ρ_c come from real cloudy images. The band correlation of thin clouds $a_{i,j}$ in (2) is determined by scattering law.

Fig. 7 shows the first simulated experiment, which is based on Landsat 8 OLI data. The main land covers are mountainous

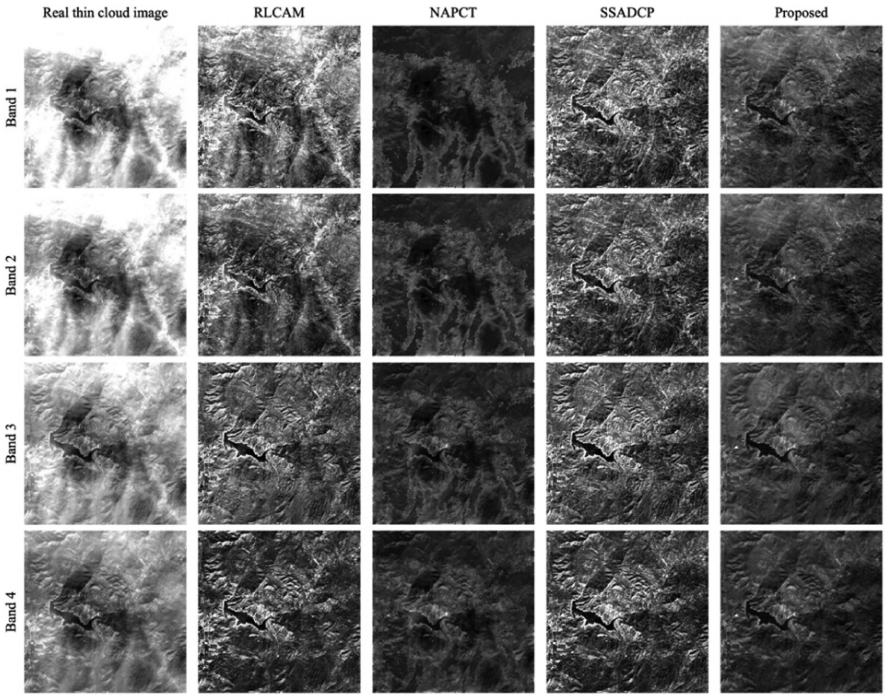

Fig. 19. Band-by-band comparison of different results. The first to the fifth columns show the visible bands (Bands 1–4 of OLI2) of the real thin cloud image, RLCAM, NAPCT, SSADCP, and proposed method, respectively.

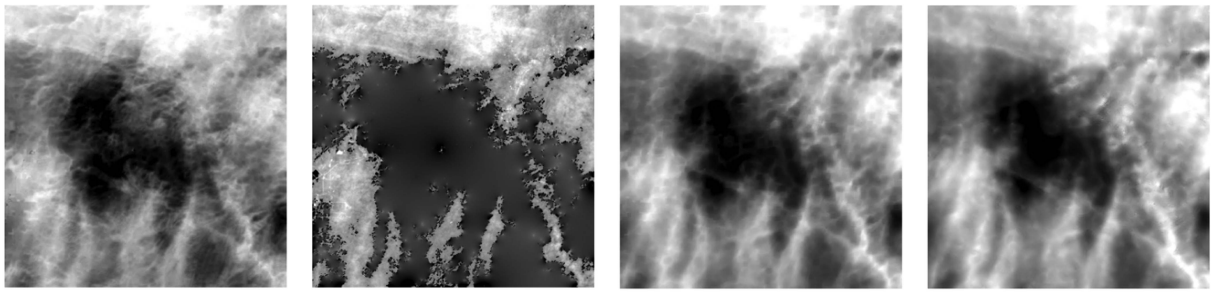

Fig. 20. Comparison of thin cloud maps produced by different methods. (a)–(d) Exhibit the thin cloud map generated from RLCAM, NAPCT, SSADCP, and the proposed method.

regions and urban areas. Fig. 7(b)–(e) shows the corrected results of RLCAM, NAPCT, SSADCP, and the proposed method, respectively. Fig. 7(f) displays the cloud-free ground truth acquired on 10 March 2022, with the numbers of path and row being 042 and 036, respectively. The individual visible band is checked for further visual comparison, as exhibited in Fig. 8. As the observation indicates, RLCAM corrects most thin clouds in the scene, and the ground surfaces are basically revealed. However, two main problems exist. RLCAM fails to correct dense thin clouds, resulting in residual clouds. Moreover, the bright surfaces in the scene are wrongly corrected, showing different colors than the ground truth. The performance of RLCAM in the scene reveals the generalizability problem of deep-learning-based methods for different data. Unlike RLCAM where the image is processed globally, NAPCT uses the cloud mask so that the spectral of cloud-free regions is untreated and well preserved. Thin clouds are also completely eliminated. Nevertheless, obvious boundaries exist between the corrected regions and cloud-free regions, degrading the visuality of the results. Different from the above methods, SSADCP can effectively remove thin clouds and recover consistent spatial and spectral characteristics as the ground truth. However, cloud traces can still be observed in the result, as indicated by the red arrow in Fig. 7(d). This finding is mainly attributed to the sparse distribution of dark targets in the scene, causing the generated thin cloud map to be insufficiently fine. As shown in Fig. 7(e), the proposed method faithfully recovers spatial and spectral details; band-by-band comparison indicates that the thin clouds in each visible band are completely corrected, suggesting a better performance than the benchmarks.

A comparison of thin cloud maps of different methods is exhibited in Fig. 9. Scatter plots between thin cloud maps and ground truth are shown in Fig. 10, where the values of RMSE

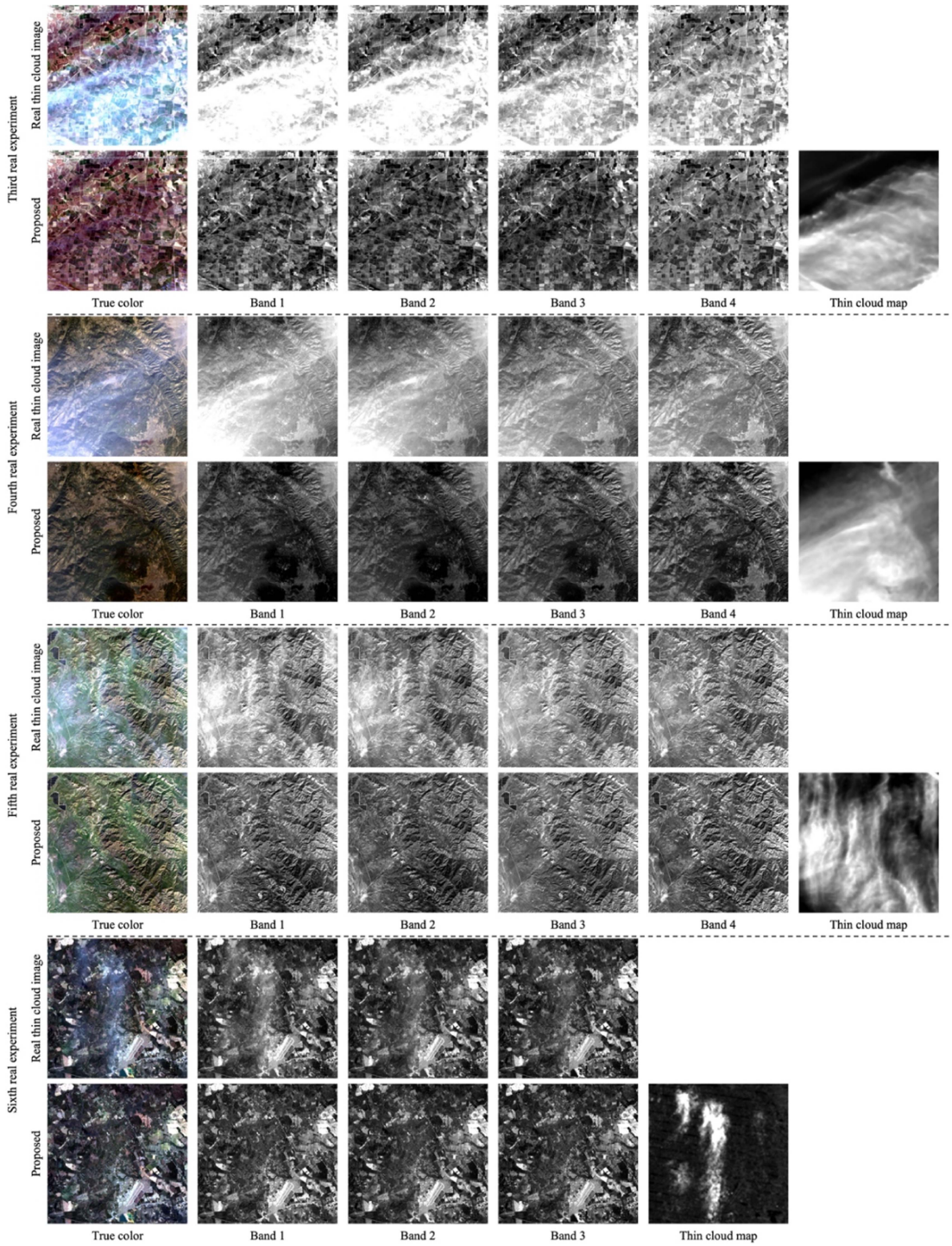

Fig. 21. Thin cloud correction results of the third to sixth real data using the proposed method.

and MAE are also given. In Fig. 9(a), RLCAM approximately estimates the thin cloud intensity in the spatial domain. Nevertheless, this approach leads to the overestimation of thin clouds over the bright surfaces in the scene, as indicated by the red ellipse. In addition, a part of the ground information is mixed in the thin cloud map, which may reduce the accuracy of the corrected result. NAPCT yields a thin cloud map with finer spatial features and few ground components. However, nonnegligible boundaries exist between the cloudy and cloud-free regions, which differs from the ground truth in Fig. 9(e). SSADCP maps thin clouds but still shows halos and block artifacts. In addition, SSADCP avoids the overestimation of thin clouds on bright surfaces, resulting in a better outcome. A thin cloud map interpolated by the proposed method is shown in Fig. 9(d). Thin clouds closely match the ground truth in both spatial distribution and intensity, as exhibited in Fig. 9(e). Furthermore, the thin

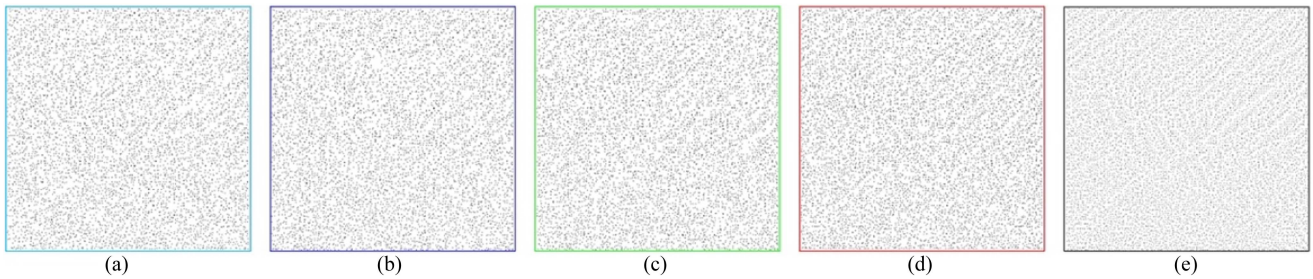

Fig. 22. Comparison of dark-object distribution in different visible bands before and after densification. (a)–(d) Dark-object distributions in bands 1–4 before densification. (e) Dark-object distribution in visible bands after densification.

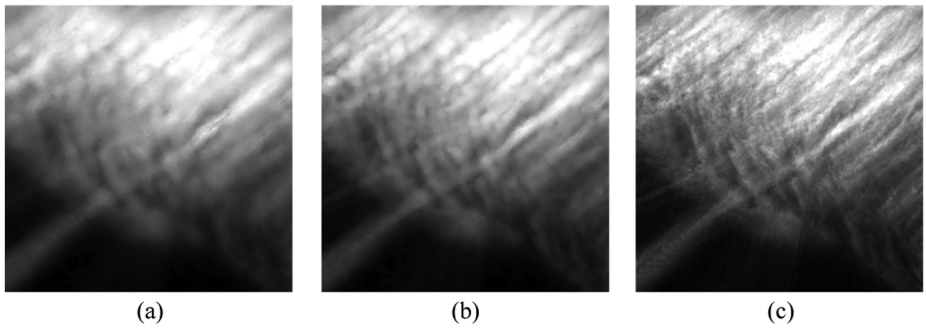

Fig. 23. Comparison of thin cloud maps interpolated from the dark objects before and after densification. (a) Thin cloud map interpolated from the dark objects without densification. (b) Thin cloud map interpolated from the densified dark objects. (c) Ground truth.

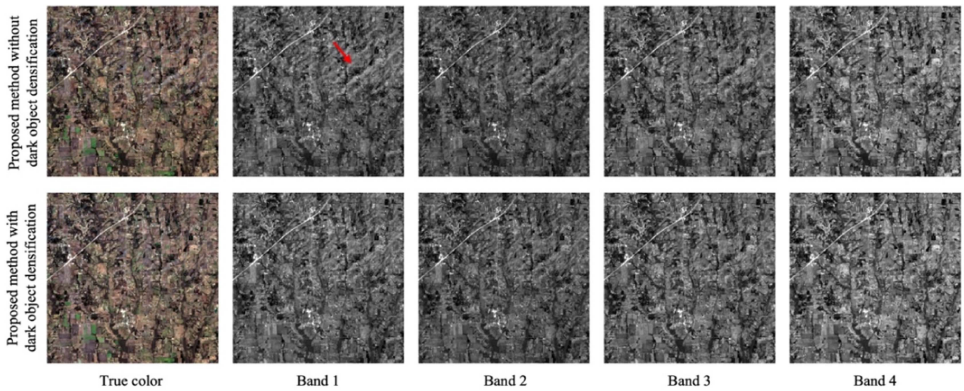

Fig. 24. Comparison of results using the proposed method with and without dark-object densification. The first to fifth columns are the true color images, bands 1–4 of OLI.

cloud map of the proposed method shows a remarkable linear correlation with the ground truth compared with the benchmarks, and the dot pairs are highly clustered around the 1:1 line, indicating low RMSE and MAE. This finding confirms that the superpixel segmentation-based dark-object location and spatial densification of dark objects promise a more accurate estimation of thin clouds, resulting in a superior corrected result.

With Fig. 7(f) as a reference, the scores of four metrics, namely, RMSE, MAE, CC, and SA, are calculated to quantitatively assess different results, as tabulated in Table I. RMSE, MAE, and CC are computed based on the individual visible bands, that is, Bands 1–4 of OLI, and SA is calculated based on all visible bands. Smaller values of RMSE, MAE, and SA indicate low data errors. A large CC value corresponds to a high data consistency. The ideal scores are presented in bold. As the table illustrates, the proposed approach achieves superior scores in almost all metrics for visible bands, which is in accordance with the visual assessment above. Thus, the proposed approach demonstrates superior performance in quantitative aspects compared with the benchmarks, proving its efficiency in thin cloud correction.

The second simulated experiment is shown in Fig. 11. The main land covers are farmland, green vegetation, and bare soils. Thin clouds primarily occur at the top of the image, as

TABLE I
QUANTITATIVE COMPARISON OF DIFFERENT RESULTS FOR THE FIRST SIMULATED EXPERIMENT

	Band	RLCAM	NAPCT	SSADCP	Proposed
RMSE	1	0.1677	0.0411	0.0942	**0.0242**
	2	0.1142	0.0319	0.0908	**0.0307**
	3	0.0912	0.0403	0.0684	**0.0381**
	4	0.0872	0.0351	0.0535	**0.0326**
MAE	1	0.0144	0.0019	0.0130	**0.0011**
	2	0.0102	0.0093	0.0082	**0.0081**
	3	0.0091	0.0041	0.0047	**0.0014**
	4	0.0057	0.0067	0.0029	**0.0019**
CC	1	0.8102	0.7881	0.8770	**0.9427**
	2	0.8244	0.8016	0.9167	**0.9640**
	3	0.8079	0.8426	0.9450	**0.9816**
	4	0.8326	0.8991	0.9693	**0.9921**
SA	1–4	13.1771	10.6621	5.9996	**3.4556**

TABLE II
QUANTITATIVE COMPARISON OF DIFFERENT RESULTS FOR THE SECOND SIMULATED EXPERIMENT

	Band	RLCAM	NAPCT	SSADCP	Proposed
RMSE	1	0.1021	0.0278	0.1234	**0.0133**
	2	0.1006	0.0592	0.0988	**0.0571**
	3	0.0731	0.0418	0.0724	**0.0322**
	4	0.0661	0.0326	0.0626	**0.0214**
MAE	1	0.0141	0.0015	0.0152	**0.0006**
	2	0.0094	0.0026	0.0098	**0.0018**
	3	0.0040	0.0024	0.0052	**0.0021**
	4	0.0037	0.0029	0.0039	**0.0024**
CC	1	0.7121	0.7140	0.8406	**0.8875**
	2	0.7011	0.8147	0.8902	**0.9323**
	3	0.7642	0.8629	0.9308	**0.9664**
	4	0.6911	0.9122	0.9433	**0.9825**
SA	1–4	12.1417	8.7271	11.6318	**6.9767**

indicated in Fig. 11(a). Thin cloud correction results of various methods are exhibited in Fig. 11(b)–(e). Fig. 11(f) shows the cloud-free ground truth acquired on 12 January 2022, and the numbers of path and row are 027 and 037, respectively. The individual visible band is shown in Fig. 12. As in the previous experiments, these four approaches show similar performance. Most thin clouds are cleared by RLCAM, but some still remain. NAPCT retains the spectra of cloud-free regions well, and the clouds are eliminated. However, color distortion and cloud boundaries are observed. Compared with RLCAM and NAPCT, SSADCP achieves better performance in cloud correction and color maintenance. Most of the thin clouds are properly removed, and the recovered spectra are consistent with the ground truth. However, some cloud traces can still be observed. Different from the benchmark approaches, the proposed method successfully clears thin clouds in all four visible bands, leaving little cloud traces. Moreover, the result shows color consistency with the ground truth, suggesting that the spectra are correctly recovered, and the cloud-free areas are well preserved.

Thin cloud maps of various methods are provided in Fig. 13, and the corresponding scatter plots are shown in Fig. 14. As the figures show, RLCAM tends to overestimate the thin cloud intensity over bright surfaces. The thin cloud intensity in cloud-free areas is very low in NAPCTs result, but the cloud boundaries are obvious. SSADCP, which considers special treatment for typical bright surfaces, manages to avoid the overestimation of thin clouds, as shown in Fig. 13(c). Figs. 13(d) and 14(d) reveal that the thin cloud map produced by the proposed method is almost consistent with the ground truth in terms of intensity and spatial distribution and holds finer texture details compared with benchmark methods.

The quantitative assessment of the second simulated experiment is listed in Table II, where the ideal values are shown in bold. Against the benchmark approaches, the proposed method obtains superior scores across the four metrics in all visible bands. This finding confirms that the proposed approach has superior correction performance compared with that of the comparative methods and can quantitatively recover the ground information underneath the thin clouds.

In accordance with the evaluations of the above simulated experiments, our approach yields corrected results that are visually satisfactory and have high spectral fidelity, outperforming the benchmark methods to a considerable extent.

B. Real Experiments

Six thin cloud images from the real world are collected to further confirm the cloud removal ability of the method in real scenes. Fig. 15 shows the first real thin cloud image sensed by OLI on 26 March 2022, and the numbers of path and row are 042 and 036, respectively. The comparison of each visible band is exhibited in Fig. 16. The scene is mainly composed of mountain lands and some bright bare soils. The results of RLCAM, NAPCT, SSADCP, and the proposed method are displayed in Fig. 15(b)–(e). As shown in Figs. 15(b) and 16, RLCAM clears the thin clouds to a great degree, but residual clouds are seen in Band 1. Against RLCAM, NAPCT shows satisfactory performance in both cloud removal and spectral retention, whereas cloud boundaries occur in the result. SSADCP can effectively correct thin clouds in different visible bands, but cloud traces can still be observed in the result. As given in Fig. 15(e), the proposed method clears the adverse cloud effects in each visible band, and no cloud traces remain. In addition, the spectra in cloud-free areas are well maintained, and the corrected information in cloudy areas is in accordance with the surroundings, indicating that the ground features underneath the clouds are faithfully recovered.

Thin cloud maps of different methods are compared visually and given in Fig. 17. Thin clouds can be estimated through these methods but with different accuracies, similar to the simulated experiments. RLCAM is adversely influenced by bright surfaces. Obvious cloud boundaries appear in NAPCTs result. SSADCP is almost free from the effects of bright surfaces but exhibits halos and block artifacts. The thin cloud map produced by the proposed method accurately describes thin clouds with finer spatial details and contains minimal ground information. The advantages of thin cloud maps indicate that the proposed

method can produce a better corrected result in terms of visual and quantitative aspects.

The second real experiment is performed based on Landsat 9 OLI2 and shown in Fig. 18. A band-by-band comparison is exhibited in Fig. 19. The main land covers are green vegetation, water surfaces, and some bright surfaces; thin clouds cover the entire scene almost completely, which is different from the first real experiment. In RLCAMs result, thin clouds are partly corrected, and the bright surfaces are distorted. NAPCT maintains the spectral of cloud-free regions. However, some residual thin clouds are observed. SSADCP clears the thin clouds and keeps the color of the bright surface. However, the result contains some cloud traces, which can be observed from the areas indicated by the red arrow. Fig. 18(e) presents the result of the proposed approach. After the correction, thin clouds are properly cleared, and the restored spectral characteristics are similar to those in surrounding regions. In addition, as shown in Fig. 20, the thin cloud map is finer than that produced by the benchmark approaches, without halos and block artifacts. Therefore, the proposed approach has superior cloud correction and spectral maintenance abilities for visible bands.

Fig. 21 gives the corrected results of the other four real thin cloud images using the proposed method. The third and fourth real data are from Landsat 9 OLI2 on 8 January 2022, the main land covers of the former are colorful farmlands, and those of the latter are dark rocks and bare soils. The fifth real data are also collected by Landsat 9 OLI2, but the acquired data are from 14 February 2022, and its land cover is composed of vegetation and bare land. The sixth real data are selected from Landsat 7 ETM+ on 28 March 2022. In accordance with the previous experiments, the proposed method shows satisfactory correction performance in all four scenes. Thin cloud maps can be accurately estimated so that every visible band is totally corrected, and the spectra in cloud-free areas are well maintained.

In short, the above real experiments demonstrate that the proposed approach is also suitable for thin cloud data with various land covers acquired from the real world, having better cloud correction and color maintenance abilities than the three comparative methods.

IV. Discussions

Two aspects need to be further clarified in this section: the advantages of dark-object densification for generating thin cloud maps and the limitations of the proposed method in certain cases.

The major novelty of the proposed method is the utilization of complementary dark objects in visible bands to interpolate thin cloud maps with finer spatial details, thereby improving the correction results. The specific advantages of dark-object densification for thin cloud map generation are discussed. The simulated thin cloud image in Fig. 11(a) is taken as an example for validation. The numbers of dark objects in each visible band before and after densification are counted and shown in Fig. 22. As depicted in the figures, the dark objects are relatively sparse in spatial before densification, with a total of 7396 dark objects in each visible band. Among them, 2473 are ADOs, and 4923 are RDOs. After densification, the number of dark objects markedly increased to 17 242, with 2473 ADOs and 14 769 RDOs. Thus, the spatial distribution of dark objects becomes visually denser, as shown in Fig. 22(e).

The interpolated thin cloud maps are compared in Fig. 23. As shown in Fig. 23(a), the thin cloud map appears coarse with fuzzy textures. By contrast, the thin cloud map in Fig. 23(b) is finer and contains more spatial details, approaching the ground truth, as shown in Fig. 23(c). On the basis of these thin cloud maps, the corrected results are obtained and given in Fig. 24. In the first row, most of the thin clouds are cleared, but some obvious cloud traces remain because the initial thin cloud map is too coarse to accurately describe the spatial details. In the second row, thin clouds are effectively removed from different visible bands, and cloud traces are largely avoided. This improvement is due to the denser dark objects, which enable a finer thin cloud map to be generated, allowing for the interpolation of more spatial details. However, a few cloud traces appear in areas with dramatic cloud changes. This limitation occurred because thin clouds can vary in extremely small local areas, and the interpolated thin cloud map approaches but does not reach the same level of fineness as the ground truth, thereby failing to describe such small changes adequately.

Moreover, in the proposed approach, thin cloud intensity over bright surfaces is interpolated using the surrounding dark objects. Thus, the interpolation operation for scenes with large areas of bright surfaces may be unsuitable, and the corrected results can be problematic. The above problems may be solved by adding virtual dark objects using some strategies, which will be explored in future studies.

V. Conclusion

In this study, a novel thin cloud correction method was proposed for single optical remote sensing data based on complementary dark objects across multiple visible bands. Dark objects were accurately located in different visible bands using a superpixel segmentation algorithm. Two subconcepts—ADOs and RDOs—were defined to characterize the dark objects. The correlation of thin cloud intensity among visible bands was calculated by fitting the ADOs. Given the complementarity of dark objects, RDOs on the one band were densified by referring to RDOs on the other bands. The combination of ADOs and densified RDOs was then used to interpolate a fine thin cloud map with enhanced texture details for various bands. The proposed method was thoroughly evaluated through simulated and real experiments conducted on a series of Landsat images. Three representative thin cloud correction methods were selected as benchmarks for comparison. Visual and quantitative assessments demonstrated that the proposed approach effectively corrected thin clouds in various scenes, producing more natural and visually faithful results compared with those produced by the benchmark methods. The thin cloud maps generated by the proposed method were finer and contained more spatial details. Quantitative evaluations further validate the efficiency of the proposed method, as it consistently achieved ideal values across RMSE, MAE, CC, and SA metrics in most cases. The proposed approach exhibited satisfactory performance in both visual and quantitative aspects

of thin cloud correction across various land covers. In addition, the advantages of dark-object densification in thin cloud map generation were demonstrated. The densified dark objects led to a finer thin cloud map with increased spatial details, closely resembling the ground truth. In terms of application scopes, the proposed approach shows satisfactory ability in correcting thin clouds that exhibit slow spatial variations. However, it may have limitations in effectively handling thin clouds that undergo dramatic changes in tiny local areas.

ACKNOWLEDGMENT

The authors would like to thank the anonymous reviewers for their valuable comments, suggestions, and enlightenment.

REFERENCES

[1] H. Shen, H. Li, Y. Qian, L. Zhang, and Q. Yuan, "An effective thin cloud removal procedure for visible remote sensing images," *ISPRS J. Photogramm. Remote Sens.*, vol. 96, pp. 224–235, 2014.

[2] C. Long, X. Li, Y. Jing, and H. Shen, "Bishift networks for thick cloud removal with multitemporal remote sensing images," *Int. J. Intell. Syst.*, vol. 2023, 2023, Art. no. 9953198 .

[3] Y. Chen, Z. Cai, J. Yuan, and L. Wu, "A novel dense-attention network for thick cloud removal by reconstructing semantic information," *IEEE J. Sel. Topics Appl. Earth Observ. Remote Sens.*, vol. 16, pp. 2339–2351, 2023, doi: 10.1109/JSTARS.2023.3236384.

[4] Z. Xu, K. Wu, L. Huang, Q. Wang, and P. Ren, "Cloudy image arithmetic: A cloudy scene synthesis paradigm with an application to deep-learning-based thin cloud removal," *IEEE Trans. Geosci. Remote Sens.*, vol. 60, pp. 1–16, Feb. 2022, doi: 10.1109/TGRS.2021.3122253.

[5] J. Li et al., "Thin cloud removal in optical remote sensing images based on generative adversarial networks and physical model of cloud distortion," *ISPRS J. Photogramm. Remote Sens.*, vol. 166, pp. 373–389, 2020.

[6] Q. Yuan et al., "Deep learning in environmental remote sensing: Achievements and challenges," *Remote Sens. Environ.*, vol. 241, 2020, Art. no. 111716.

[7] W. Li, Y. Li, D. Chen, and J. C.-W. Chan, "Thin cloud removal with residual symmetrical concatenation network," *ISPRS J. Photogramm. Remote Sens.*, vol. 153, pp. 137–150, 2019.

[8] X. Wen, Z. Pan, Y. Hu, and J. Liu, "An effective network integrating residual learning and channel attention mechanism for thin cloud removal," *IEEE Geosci. Remote Sens. Lett.*, vol. 19, pp. 1–5, 2022, doi: 10.1109/LGRS.2022.3161062.

[9] M. Xu, F. Deng, S. Jia, X. Jia, and A. J. Plaza, "Attention mechanism-based generative adversarial networks for cloud removal in Landsat images," *Remote Sens. Environ.*, vol. 271, 2022, Art. no. 112902.

[10] Y. Du, B. Guindon, and J. Cihlar, "Haze detection and removal in high resolution satellite image with wavelet analysis," *IEEE Trans. Geosci. Remote Sens.*, vol. 40, no. 1, pp. 210–217, Jan. 2002.

[11] J. Liu et al., "Thin cloud removal from single satellite images," *Opt. Exp.*, vol. 22, no. 1, pp. 618–632, 2014.

[12] J. Li, Q. Hu, and M. Ai, "Haze and thin cloud removal via sphere model improved dark channel prior," *IEEE Geosci. Remote Sens. Lett.*, vol. 16, no. 3, pp. 472–476, Mar. 2019.

[13] Y. Zi, H. Ding, F. Xie, Z. Jiang, and X. Song, "Wavelet integrated convolutional neural network for thin cloud removal in remote sensing images," *Remote Sens.*, vol. 15, no. 3, 2023, Art. no. 781.

[14] Y. Zhang, B. Guindon, and J. Cihlar, "An image transform to characterize and compensate for spatial variations in thin cloud contamination of Landsat images," *Remote Sens. Environ.*, vol. 82, no. 2/3, pp. 173–187, 2002.

[15] C. Zhang, P. Yi, Y. Liu, L. Ma, W. Hu, and J. Wu, "Thin cloud correction method for visible remote sensing images using a spectral transformation scheme," *GIScience Remote Sens.*, vol. 60, no. 1, 2023, Art. no. 2196133.

[16] E. P. Crist and R. C. Cicone, "A physically-based transformation of thematic mapper data—The TM tasseled cap," *IEEE Trans. Geosci. Remote Sens.*, vol. GE-22, no. G-3, pp. 256–263, May 1984.

[17] Y. Shen, Y. Wang, H. Lv, and J. Qian, "Removal of thin clouds in Landsat-8 OLI data with independent component analysis," *Remote Sens.*, vol. 7, no. 9, pp. 11481–11500, 2015.

[18] H. Li, L. Zhang, and H. Shen, "A principal component based haze masking method for visible images," *IEEE Geosci. Remote Sens. Lett.*, vol. 11, no. 5, pp. 975–979, May 2014.

[19] M. Xu, X. Jia, M. Pickering, and S. Jia, "Thin cloud removal from optical remote sensing images using the noise-adjusted principal components transform," *ISPRS J. Photogramm. Remote Sens.*, vol. 149, pp. 215–225, 2019.

[20] R. K. Vincent, "An ERTS multispectral scanner experiment for mapping iron compounds," Tech. Rep. E72-10181, 1972.

[21] P. S. Chavez Jr., "An improved dark-object subtraction technique for atmospheric scattering correction of multispectral data," *Remote Sens. Environ.*, vol. 24, no. 3, pp. 459–479, 1988.

[22] A. Makarau, R. Richter, R. Müller, and P. Reinartz, "Haze detection and removal in remotely sensed multispectral imagery," *IEEE Trans. Geosci. Remote Sens.*, vol. 52, no. 9, pp. 5895–5905, Sep. 2014.

[23] K. He, J. Sun, and X. Tang, "Single image haze removal using dark channel prior," *IEEE Trans. Pattern Anal. Mach. Intell.*, vol. 33, no. 12, pp. 2341–2353, Dec. 2011.

[24] H. Shen, C. Zhang, H. Li, Q. Yuan, and L. Zhang, "A spatial–spectral adaptive haze removal method for visible remote sensing images," *IEEE Trans. Geosci. Remote Sens.*, vol. 58, no. 9, pp. 6168–6180, Sep. 2020.

[25] C. Zhang et al., "A general thin cloud correction method combining statistical information and a scattering model for visible and near-infrared satellite images," *IEEE Trans. Geosci. Remote Sens.*, vol. 61, Jul. 2023, Art. no. 5405019.

[26] M. Xu, M. Pickering, A. J. Plaza, and X. Jia, "Thin cloud removal based on signal transmission principles and spectral mixture analysis," *IEEE Trans. Geosci. Remote Sens.*, vol. 54, no. 3, pp. 1659–1669, Mar. 2016.

[27] H. Lv, Y. Wang, and Y. Shen, "An empirical and radiative transfer model based algorithm to remove thin clouds in visible bands," *Remote Sens. Environ.*, vol. 179, pp. 183–195, 2016.

[28] C. Zhang, H. Li, and H. Shen, "A scattering law based cirrus correction method for Landsat 8 OLI visible and near-infrared images," *Remote Sens. Environ.*, vol. 253, 2021, Art. no. 112202.

[29] E. J. McCartney, "Optics of the atmosphere: Scattering by molecules and particles," New York, NY, USA, 1976.

[30] P. S. Chavez Jr., "Radiometric calibration of Landsat thematic mapper multispectral images," *Photogramm. Eng. Remote Sens.*, vol. 55, no. 9, pp. 1285–1294, 1989.

Peng Yi received the B.S. degree in surveying and mapping engineering from Wuhan University, Wuhan, China, in 2005.

He is currently the Head of Huadu Branch, Guangzhou Urban Planning and Design Survey Research Institute, Guangzhou, China. He is also a senior surveying and mapping Engineer. His research interests include urban renewal, engineering surveying, and image processing.

Chi Zhang (Member, IEEE) received the B.S. degree in surveying and mapping engineering from Hohai University, Nanjing, China, in 2016, and the Ph.D. degree in cartography and geographical information engineering from Wuhan University, Wuhan, China, in 2021.

He is currently a surveying and mapping Engineer with Guangzhou Urban Planning and Design Survey Research Institute, Guangzhou, China. His research interests include optical data intelligent processing and city environmental monitoring.

Li Ma received the M.S. degree in surveying and mapping engineering from the Chinese Academy of Sciences, Wuhan, China, in 2014.

He is a senior surveying and mapping Engineer with Huadu Branch, Guangzhou Urban Planning and Design Survey Research Institute, Guangzhou, China. His research interests include urban renewal, engineering surveying, and image processing.

Yang Liu received the Ph.D. degree in cartography and geographic information system from Wuhan University, Wuhan, China, in 2008.

He is currently the Chief Engineer and the Head of Technology Department, Guangzhou Urban Planning and Design Survey Research Institute, Guangzhou, China. He is also a Registered Surveyor, Registered Planner, and Professional Engineer. His research interests include spatial data mining and disaster prediction.

Huagui He received the B.S. degree in cartography from Wuhan University, Wuhan, China, in 2000.

He is currently the Director of Geographic Information Center, Guangzhou Urban Planning and Design Survey Research Institute, Guangzhou, China. He is also a professional senior surveying and mapping Engineer. His research interests include smart city, computer cartography, and image processing.

Wenxiong Hu received the B.S. degree in surveying and mapping engineering from Wuhan University, Wuhan, China, in 2012.

He is a senior surveying and mapping Engineer with Huadu Branch, Guangzhou Urban Planning and Design Survey Research Institute, Guangzhou, China. His research interests include urban renewal, engineering surveying, and image processing.